

REPORT DOCUMENTATION PAGE				Form Approved OMB No. 0704-0188	
Public reporting burden for this collection of information is estimated to average 1 hour per response, including the time for reviewing instructions, searching existing data sources, gathering and maintaining the data needed, and completing and reviewing this collection of information. Send comments regarding this burden estimate or any other aspect of this collection of information, including suggestions for reducing this burden to Department of Defense, Washington Headquarters Services, Directorate for Information Operations and Reports (0704-0188), 1215 Jefferson Davis Highway, Suite 1204, Arlington, VA 22202-4302. Respondents should be aware that notwithstanding any other provision of law, no person shall be subject to any penalty for failing to comply with a collection of information if it does not display a currently valid OMB control number. PLEASE DO NOT RETURN YOUR FORM TO THE ABOVE ADDRESS.					
1. REPORT DATE (DD-MM-YYYY) 31-05-2006		2. REPORT TYPE Technical Paper		3. DATES COVERED (From - To)	
4. TITLE AND SUBTITLE 2D Electrostatic Potential Solver for Hall Thruster Simulation				5a. CONTRACT NUMBER	
				5b. GRANT NUMBER	
				5c. PROGRAM ELEMENT NUMBER	
6. AUTHOR(S) Justin W. Koo (Advatech Pacific, Inc.)				5d. PROJECT NUMBER 48470052	
				5e. TASK NUMBER	
				5f. WORK UNIT NUMBER	
7. PERFORMING ORGANIZATION NAME(S) AND ADDRESS(ES) Air Force Research Laboratory (AFMC) AFRL/PRSS 1 Ara Drive Edwards AFB CA 93524-7013				8. PERFORMING ORGANIZATION REPORT NUMBER AFRL-PR-ED-TP-2006-168	
9. SPONSORING / MONITORING AGENCY NAME(S) AND ADDRESS(ES) Air Force Research Laboratory (AFMC) AFRL/PRS 5 Pollux Drive Edwards AFB CA 93524-70448				10. SPONSOR/MONITOR'S ACRONYM(S)	
				11. SPONSOR/MONITOR'S NUMBER(S) AFRL-PR-ED-TP-2006-168	
12. DISTRIBUTION / AVAILABILITY STATEMENT Approved for public release; distribution unlimited (AFRL-ERS-PAS-2006-115)					
13. SUPPLEMENTARY NOTES Presented at the 42 nd AIAA/ASME/SAE/ASEE Joint Propulsion Conference, Sacramento, CA, 9-12 July 2006.					
14. ABSTRACT This paper presents the formulation of a 2D axisymmetric electrostatic potential solver (2DFV) for Hall thruster simulation. It is based on a finite volume discretization of a current conservation equation where the electron current density is described by a Generalized Ohm's law description. Comparison of 2DFV to an existing 1D axisymmetric electrostatic potential solver is provided and investigation is performed into anomalous mobility corrections and Hall current calculation. Details of an extension of this formulation to include $\vec{j} \times \vec{B}$ plasma turbulence terms are also provided.					
15. SUBJECT TERMS					
16. SECURITY CLASSIFICATION OF:			17. LIMITATION OF ABSTRACT A	18. NUMBER OF PAGES 15	19a. NAME OF RESPONSIBLE PERSON Dr. Brian Beal
a. REPORT Unclassified	b. ABSTRACT Unclassified	c. THIS PAGE Unclassified			19b. TELEPHONE NUMBER (include area code) N/A

2D electrostatic potential solver for Hall thruster simulation

Justin W. Koo*

This paper presents the formulation of a 2D axisymmetric electrostatic potential solver (2DFV) for Hall thruster simulation. It is based on a finite volume discretization of a current conservation equation where the electron current density is described by a Generalized Ohm's law description. Comparison of 2DFV to an existing 1D axisymmetric electrostatic potential solver is provided and investigation is performed into anomalous mobility corrections and Hall current calculation. Details of an extension of this formulation to include $\vec{j} \times \vec{B}$ plasma turbulence terms are also provided.

Nomenclature

\vec{j}	Current density, A/m^2
\vec{j}_i	Ion current density, A/m^2
\vec{j}_e	Electron current density, A/m^2
μ	Electron mobility, $m^2/V/s$
\vec{B}	Magnetic field, T
n_e	Plasma density, $1/m^3$
n_{xe}	Neutral density, $1/m^3$
\vec{E}	Electric field, V/m
p	Plasma pressure, Pa
$\vec{\alpha}$	Cross-correlation terms, $A \cdot T/m^2$
\hat{n}	Normal vector (pointing out of cell)
T_e	Electron temperature, K
v_{th}	Electron thermal velocity, m/s
ν_{en}	Electron-neutral elastic collision frequency, 1/s
Ω	Hall parameter
m_{xe}	Xenon mass, 2.15E-25 kg
m_e	Electron mass, 9.11E-31 kg
q_e	Electron charge, 1.602E-19 C
k_b	Boltzmann constant, 1.3807E-23 J/K
d_c	Acceleration channel width, 0.025 m

I. Introduction

Modern Hall thruster device simulation codes, including those by Fife,¹ Hagelaar,² and Koo³ use potential solver formulations which rely on the concept of the thermalized potential (pioneered by Morozov⁴) to discretize a multidimensional physical domain into a single quasi-axial dimension demarcated by magnetic field lines. This formulation has proven to be very successful but relies on the strict assumption of isothermal electrons along magnetic field lines and is difficult to adapt to certain magnetic field geometries. The formulation of a 2D finite volume potential solver based on the same concept of current conservation is explored in this paper and comparisons are provided to demonstrate the additional physics which can be explored with a true 2D formulation.

*Engineer, Advatech Pacific, Inc., Palmdale, CA, 93550, and AIAA Member.

II. Current conservation

Since 2DFV is designed for use with a hybrid-PIC code where the timestep is much larger than the time necessary for the electric field to equilibrate to the plasma conditions, the simplified steady-state version of current conservation, shown in Eqn. 1, is applicable.

$$\nabla \cdot \vec{j} = \nabla \cdot (\vec{j}_i + \vec{j}_e) = 0 \quad (1)$$

When incorporated into hybrid PIC codes, the ion current density can be tracked directly via the macroparticles motion while the electron current density is derived from a generalized Ohm's Law formulation.

III. Generalized Ohm's law

The electron current density is based on the following generalized Ohm's Law formulation:

$$\vec{j}_e = \mu(\vec{j}_e \times \vec{B}) + \mu ne \vec{E} + \mu \vec{\nabla} p \quad (2)$$

Expanding Eqn. 2, a set of three equations can be written for the electron current in the axial, radial, and azimuthal directions (dropping the subscript e for convenience).

$$\begin{aligned} j_z &= \mu(j_\theta B_r - j_r B_\theta) + \mu ne E_z + \mu \nabla_z p \\ j_r &= \mu(j_z B_\theta - j_\theta B_z) + \mu ne E_r + \mu \nabla_r p \\ j_\theta &= \mu(j_r B_z - j_z B_r) + \mu ne E_\theta + \mu \nabla_\theta p \end{aligned} \quad (3)$$

Due to the axisymmetric geometry of the Hall thruster, the electric field and gradient of the pressure in the azimuthal direction are identically zero. With this simplification, the azimuthal electron current density is no longer a function of any azimuthal quantities and is written as:

$$j_\theta = \mu(j_r B_z - j_z B_r) \quad (4)$$

It is now possible to substitute j_θ into the equations for the axial and radial electron current density. This leads to the following set of coupled linear equations:

$$\begin{aligned} j_z &= \mu(\mu(j_r B_z - j_z B_r) B_r - j_r B_\theta) + \mu ne E_z + \mu \nabla_z p \\ j_r &= \mu(j_z B_\theta - \mu(j_r B_z - j_z B_r) B_z) + \mu ne E_r + \mu \nabla_r p \end{aligned} \quad (5)$$

This equation system can be solved to isolate the axial and radial components of the electric current density:

$$\begin{aligned} j_z &= \mu_{11}(\mu ne E_z + \mu \nabla_z p) + \mu_{12}(\mu ne E_r + \mu \nabla_r p) \\ j_r &= \mu_{21}(\mu ne E_z + \mu \nabla_z p) + \mu_{22}(\mu ne E_r + \mu \nabla_r p) \end{aligned} \quad (6)$$

where,

$$\begin{aligned} \mu_{11} &= \frac{1 + \mu^2 B_z^2}{1 + \mu^2 B^2} \\ \mu_{12} &= \frac{\mu B_\theta + \mu^2 B_r B_z}{1 + \mu^2 B^2} \\ \mu_{21} &= \frac{-\mu B_\theta + \mu^2 B_r B_z}{1 + \mu^2 B^2} \\ \mu_{22} &= \frac{1 + \mu^2 B_r^2}{1 + \mu^2 B^2} \end{aligned} \quad (7)$$

and,

$$\mu = \frac{q_e}{m_e \nu} \quad (8)$$

Clearly, in the limit of $B_r = B$ and $B_z = B_\theta = 0$, the mobility coefficients return to their desired classical forms:

$$\begin{aligned} \mu_{11}\mu &= \mu_\perp = \frac{\mu}{1 + \mu^2 B^2} \\ \mu_{12}\mu &= 0 \\ \mu_{21}\mu &= 0 \\ \mu_{22}\mu &= \mu_\parallel = \mu \end{aligned} \quad (9)$$

Simplification

The following simplifications are used to more easily manipulate the equation system.

$$\begin{aligned} j_z &= Z_3 E_z + Z_4 E_r + Z_5 \\ j_r &= R_3 E_z + R_4 E_r + R_5 \end{aligned} \quad (10)$$

where,

$$\begin{aligned} Z_5 &= enu_{iz} + \mu_{11}\mu \nabla_z p + \mu_{12}\mu \nabla_r p \\ Z_3 &= \mu_{11}\mu ne \\ Z_4 &= \mu_{12}\mu ne \end{aligned} \quad (11)$$

and,

$$\begin{aligned} R_5 &= enu_{ir} + \mu_{21}\mu \nabla_z p + \mu_{22}\mu \nabla_r p \\ R_3 &= \mu_{21}\mu ne \\ R_4 &= \mu_{22}\mu ne \end{aligned} \quad (12)$$

IV. Finite-Volume discretization

To formulate the numerical scheme used in 2DFV, integrate Eqn. 1 over the cell area as follows:

$$\int_V \nabla \cdot \vec{j} \partial V = \int_V 0 \partial V = 0 \quad (13)$$

Using the divergence theorem, this equation becomes:

$$\int_S \vec{j} \cdot \hat{n} \partial S = 0 \quad (14)$$

Eqn. 14 clearly demonstrates that 2DFV simply balances the current fluxes into and out of a given cell. This formulation is well suited to “noisy” density profiles produced by particle codes because it contains no derivatives higher than first order for the plasma pressure term.

A. Computational stencil

The acceleration channel of the Hall thruster (shown in Fig. 1) is mapped with a cartesian mesh. The electrostatic potential is stored at the cell-centers of this grid ($n_z \times n_r$ cells) while the electric field values (both axial and radial) are stored on staggered EW and NS grids offset from the main cartesian mesh by $\Delta r/2$ and $\Delta z/2$, respectively. The electric field values on the EW grid ($n_z+1 \times n_r$ nodes) are face-centered axially

and cell-centered radially and those on the NS grid ($n_z \times n_r + 1$) are cell-centered axially and face-centered radially. Discretizing Eqn. 14 leads to the following simple identity:

$$j_z^E \Delta A_{east} - j_z^W \Delta A_{west} + j_r^N \Delta A_{north} - j_r^S \Delta A_{south} = 0 \quad (15)$$

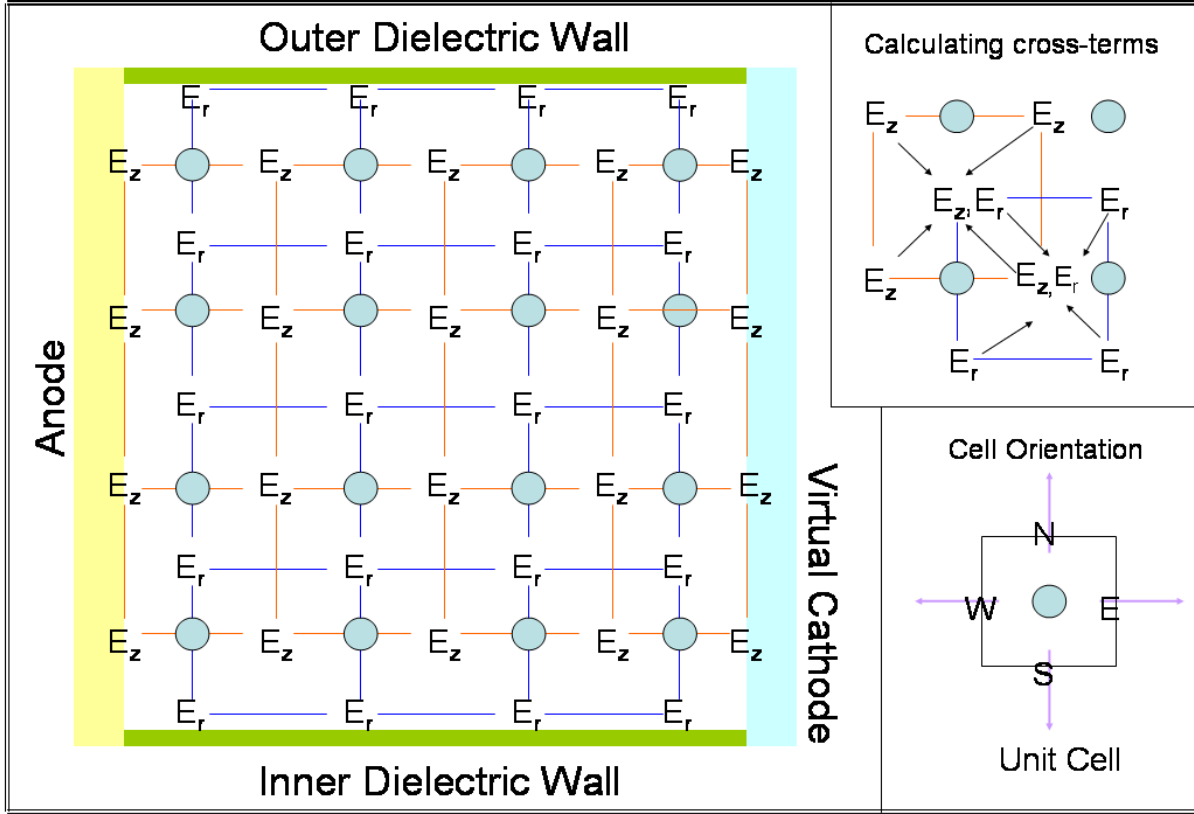


Figure 1. Computational Stencil - (main figure) circles represent cell-centered potential values, orange lines represents EW grid, blue lines represents NS grid; (upper right inset) moving electric field values from NS to EW grid and vice versa; (lower right inset) purple lines represent cell normal directions

Using the simplifications described in Sec. III, Eqn. 16 can be obtained:

$$\begin{aligned} & Z_5^E \Delta A_{east} + Z_3^E E_Z^E \Delta A_{east} + Z_4^E E_R^E \Delta A_{east} - Z_5^W \Delta A_{west} - Z_3^W E_Z^W \Delta A_{west} - Z_4^W E_R^W \Delta A_{west} \\ & + R_5^N \Delta A_{north} + R_3^N E_Z^N \Delta A_{north} + R_4^N E_R^N \Delta A_{north} - R_5^S \Delta A_{south} - R_3^S E_Z^S \Delta A_{south} - R_4^S E_R^S \Delta A_{south} = 0 \end{aligned} \quad (16)$$

One challenge to solving this equation is how to discretize the “cross” terms, such as E_R^E and E_Z^S . The approach used in 2DFV consists of moving these cross terms to the RHS of the equation (along with the electric field-free terms) and solving for them iteratively. This leaves only four electric field terms on the LHS, corresponding to the normal field on each of the four faces. The resulting equation is as follows:

$$\begin{aligned} & Z_3^E E_Z^E \Delta A_{east} - Z_3^W E_Z^W \Delta A_{west} + R_4^N E_R^N \Delta A_{north} - R_4^S E_R^S \Delta A_{south} = \\ & -(Z_5^E + Z_4^E E_R^E) \Delta A_{east} + (Z_5^W + Z_4^W E_R^W) \Delta A_{west} - (R_5^N + R_3^N E_Z^N) \Delta A_{north} + (R_5^S + R_3^S E_Z^S) \Delta A_{south} \end{aligned} \quad (17)$$

The face-centered electric fields on the LHS of Eqn. 17 can be expanded using the cell-centered potentials as follows:

$$\begin{aligned}
E_Z^E &= -\frac{\phi^{i+1,j} - \phi^{i,j}}{\Delta z} \\
E_Z^W &= -\frac{\phi^{i,j} - \phi^{i-1,j}}{\Delta z} \\
E_R^N &= -\frac{\phi^{i,j+1} - \phi^{i,j}}{\Delta r} \\
E_R^S &= -\frac{\phi^{i,j} - \phi^{i,j-1}}{\Delta r}
\end{aligned} \tag{18}$$

With appropriate boundary conditions, a pentadiagonal linear system of equations of the form $Ax=b$ can be constructed (where x is the solution vector for the potential). This equation is iterated until the L_2 -norm of the difference in the potential field between two iterations is less than 0.001. For more complete convergence studies, see Appendix B. It is important to note that because this potential solver is cell-based, the resulting electric field can be calculated only on the interior nodes. Special treatment is necessary to obtain the electric field on the boundary nodes. A flow diagram summarizing 2DFV execution is presented in Fig. 2.

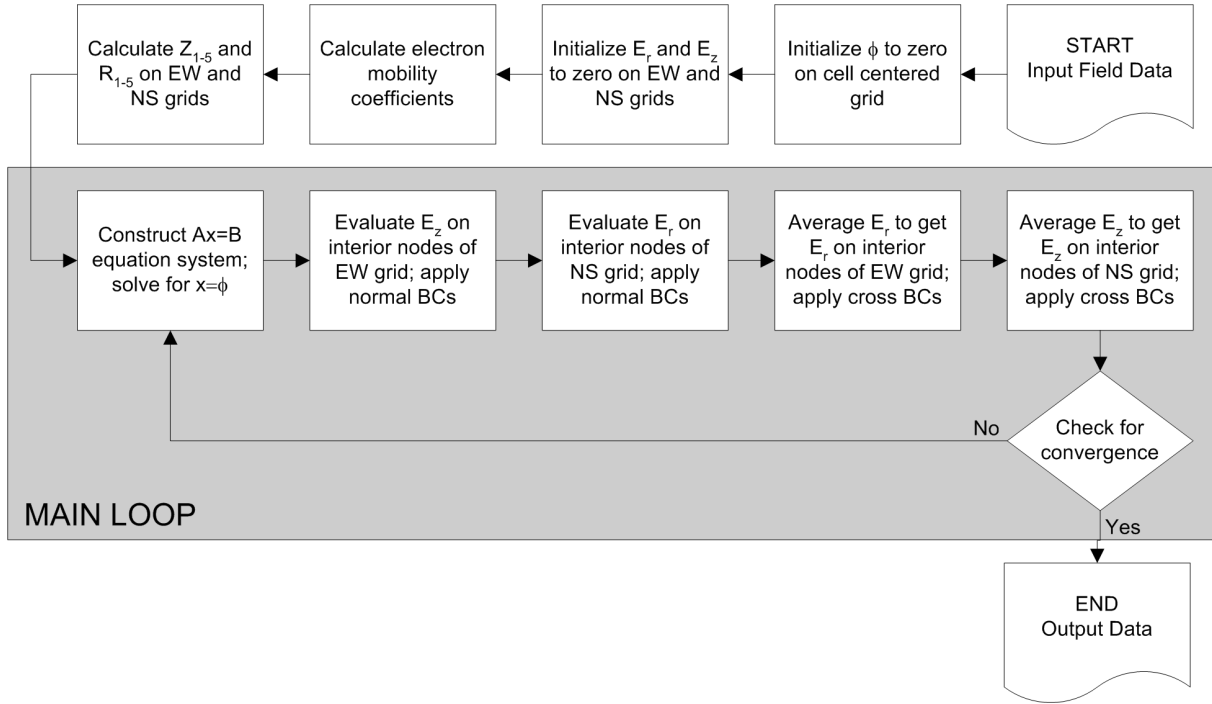


Figure 2. Flow Diagram for Potential Solver

B. Boundary conditions for linear system

Appropriate boundary conditions are necessary to obtain the correct A matrix for the linear equation solve step. Dirichlet potential conditions at the anode and virtual cathode can be implemented directly into Eqn. 18. On the inner and outer walls, Eqn. 15 is modified by setting j_r^S and j_r^N equal to zero, respectively. At corner points, both of these conditions are satisfied simultaneously.

C. Boundary conditions for electric field

As shown in Fig. 2, separate boundary conditions are needed to establish the electric field on the boundary nodes for both normal and cross boundary conditions. These normal boundary conditions correspond to E_z

conditions on the EW grid and E_r conditions on the NS grid. The E_z^{EW} BC couples directly to the Dirichlet potential conditions at the anode and virtual cathode. The E_r^{NS} BC, representing the radial force on the plasma towards or away from the walls, would be an ideal location to implement a presheath correction; however, for the results presented in this paper, the E_r^{NS} BC is simply the value of E_r on the adjacent interior node of the NS grid.

The cross boundary conditions correspond to E_r conditions on the EW grid and E_z conditions on the NS grid. The E_r^{EW} BC is calculated directly from the Dirichlet potential conditions at the anode and virtual cathode. (For a perfectly conducting anode, this would translate to an E_r^{EW} BC of exactly zero.) The E_z^{NS} BC represents the axial force on the plasma along the dielectric wall. Since no axial presheath physics are considered in 2DFV, the E_z^{NS} BC is simply the value of E_z on the adjacent interior node of the NS grid.

D. Implementation details

The results presented in this paper were produced using MATLAB 7.0. Sparse matrix structures were used to store the coefficient matrices A and B. Solution time was typically on the order of 5-25 seconds (for 200-750 iterations) on a 40x40 node grid. When coupled into a full hybrid-PIC code, it is estimated that fewer iterations will be needed since the initial guess for the potential field from the previous timestep should be close to convergence if the plasma conditions are not vastly different. It should also be noted that MATLAB is a comparatively slow interpreted language and significant speedup is expected when this code is ported to C++.

V. Results and Discussion

Two major themes are explored in this section - the sensitivity of the solution to the anomalous mobility correction and uncertainty in Hall current calculation. The results presented in this paper are based on the plasma density, neutral density, ion velocity, and electron temperature profiles presented in Fig. 3. These are instantaneous plasma properties from a simulation of HPHall, developed by Fife,¹ using a Bohm-mobility correction to the anomalous mobility. The magnetic field profile and corresponding electrostatic potential profile (based on the quasi-1D potential solver in HPHall) are presented in Fig. 4.

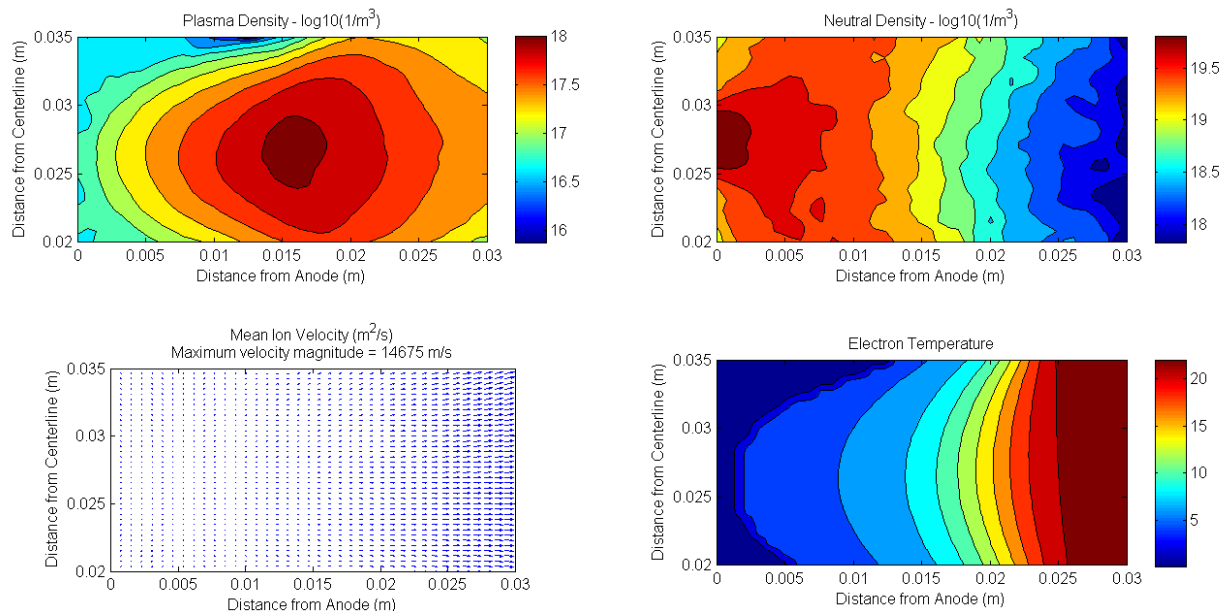


Figure 3. Initial data profiles

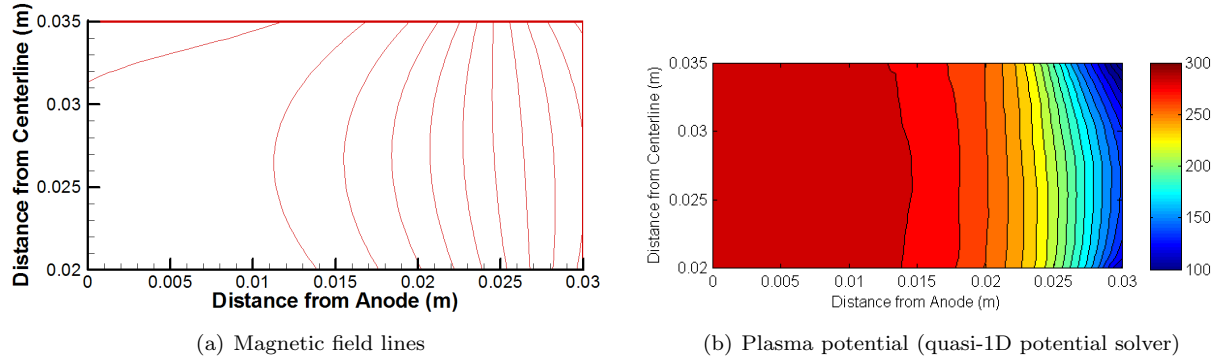


Figure 4. Field profiles from HPHall

Classical mobility

Traditionally, the principal electron collision mechanism which impacts the electron mobility is electron-neutral elastic scattering. The simple formulation used in 2DFV is as follows:

$$\nu = \nu_{en} = 2.15E - 13 \cdot n_{xe} \quad (19)$$

Anomalous mobility

The addition of anomalous mobility to Hall thruster codes has been attempted through both direct addition to the mobility term by Fife:¹

$$\mu = \mu_{classical} + \mu_{anom} \quad (20)$$

and also through increasing the effective electron elastic collision frequency by Boeuf:⁵

$$\nu = \nu_{en} + \nu_{anom} \quad (21)$$

In the framework of 2DFV, the second type of correction is used. The particular form of this anomalous mobility correction is based on the idea that the electron can “jump” field lines by scattering off the dielectric wall sheath. The form of the wall-based anomalous mobility correction used in this code is:

$$\nu_{anom} = \alpha \frac{v_{th}}{d_c} \quad (22)$$

This form includes a modeling coefficient α and the definition of the local electron thermal velocity as,

$$v_{th} = \sqrt{\frac{8k_b T_e}{\pi m_e}} \quad (23)$$

A. Sensitivity

Potential profiles and mobility coefficients for a range of α from 0.0 to 0.8 are presented in Fig. 5 and Fig. 6. The ratio of the parallel to perpendicular mobility in Eqn. 9 (assuming a ratio of $\mu B \gg 1$) can be approximated by:

$$\frac{\mu_{\parallel}}{\mu_{\perp}} \sim \left(\frac{1}{\nu} \right)^2 \quad (24)$$

One implication of this relationship is that as the mobility ratio increases the potential solution should closely resemble the magnetic field lines. Classical mobility represents the lowest reasonable bounds for ν and thus the highest possible mobility ratio expected in a Hall thruster simulation. This behavior is evident in the resemblance of Fig. 5(a) to the magnetic field lines presented in Fig. 4.

An additional result of note is the change in the orientation of the equipotential line (most evident in Fig. 5(i)) near the outer dielectric wall between 0.01 and 0.015 m from the anode. The behavior reflects the

local drop in the plasma density which is evident in Fig. 3(a). This steep gradient in plasma density translates to a strong $\nabla_r p$ force and a corresponding steep potential gradient in the radial direction. Capturing such 2D effects is not always possible with a quasi-1D potential solver.

Table 1. Current measured at Virtual Cathode

α	I_i (A)	I_e (A)	I_d (A)
0.800	1.3057	4.5503	5.8559
0.600	1.3057	3.4117	4.7173
0.400	1.3057	2.2564	3.562
0.200	1.3057	1.1147	2.4204
0.100	1.3057	0.63863	1.9443
0.075	1.3057	0.60419	1.9098
0.050	1.3057	0.75488	2.0605
0.025	1.3057	1.7935	3.0992
0.000	1.3057	19.174	20.48

The anomalous mobility correction has a significant impact on the magnitude of the electron current (and thus on the discharge current and thruster efficiency). The sensitivity of the electron and discharge currents to the anomalous mobility correction are presented in the Table 1. The minimum in the discharge current observed around $\alpha=0.075$ can be interpreted by considering the following notional relationship between the electron mobility and electric field:

$$I_e \sim \mu \cdot n_e E \quad (25)$$

In the limit of classical mobility, there is a significant potential drop in the vicinity of the peak plasma density so the $n_e E$ term is fairly large. Furthermore, the large cross mobility (μ_{12}) term also contributes to a very high axial electron current. These effects diminish with the addition of anomalous mobility. By contrast, the addition of the anomalous mobility correction directly elevates the electron current. Not surprisingly, somewhere between these limits for the mobility correction (in this case, around $\alpha=0.075$), a minimum exists in the discharge current. This behavior, while completely reasonable in the context of a steady state potential solver with fixed plasma conditions, is not necessarily physically realistic in a time-dependent solution due to the ability of the plasma to respond to the potential gradient.

B. Hall current

The Hall current density is a very difficult parameter to measure experimentally; however, from simulation data it can be calculated in at least two ways. The Hall current density can be calculated directly from Eqn. 4 (“ j_θ ”) or from the ExB drift as follows (“ j_{ExB} ”):

$$j_{ExB} = -q_e n_e (\vec{E} \times \vec{B})|_\theta = -q_e n_e \frac{E_r B_z - E_z B_r}{|B|^2} \quad (26)$$

The integrated Hall current from the two approaches and the corresponding Hall parameters (ratio of Hall current to discharge current) are provided in Table 2. These results demonstrate fundamentally different plasma behavior. The j_θ approach relies very heavily on the magnitude of the electron mobility. Since the anomalous correction directly raises or lowers this value, it also serves to very strongly adjust the magnitude of the j_θ -based Hall parameter. The j_{ExB} approach does not have this same strong dependence on the anomalous mobility correction. Since the potential profiles are bounded by the anode and virtual cathode potentials and thus show limited change with the α parameter, it is not surprising that the j_{ExB} -based Hall parameters shows much smaller variation over the same range of anomalous mobility corrections.

The location of the Hall current for the cases of $\alpha = 0.075$ and $\alpha = 0.600$, provided in Fig. 7, clearly indicates very different behavior for the two different methods of calculating the Hall current density. When calculated using j_{ExB} , the highest Hall current density exists in the center of the acceleration channel due to the high plasma density (as shown in Fig. 3(a)) in the interior of the thruster. By contrast, when calculated

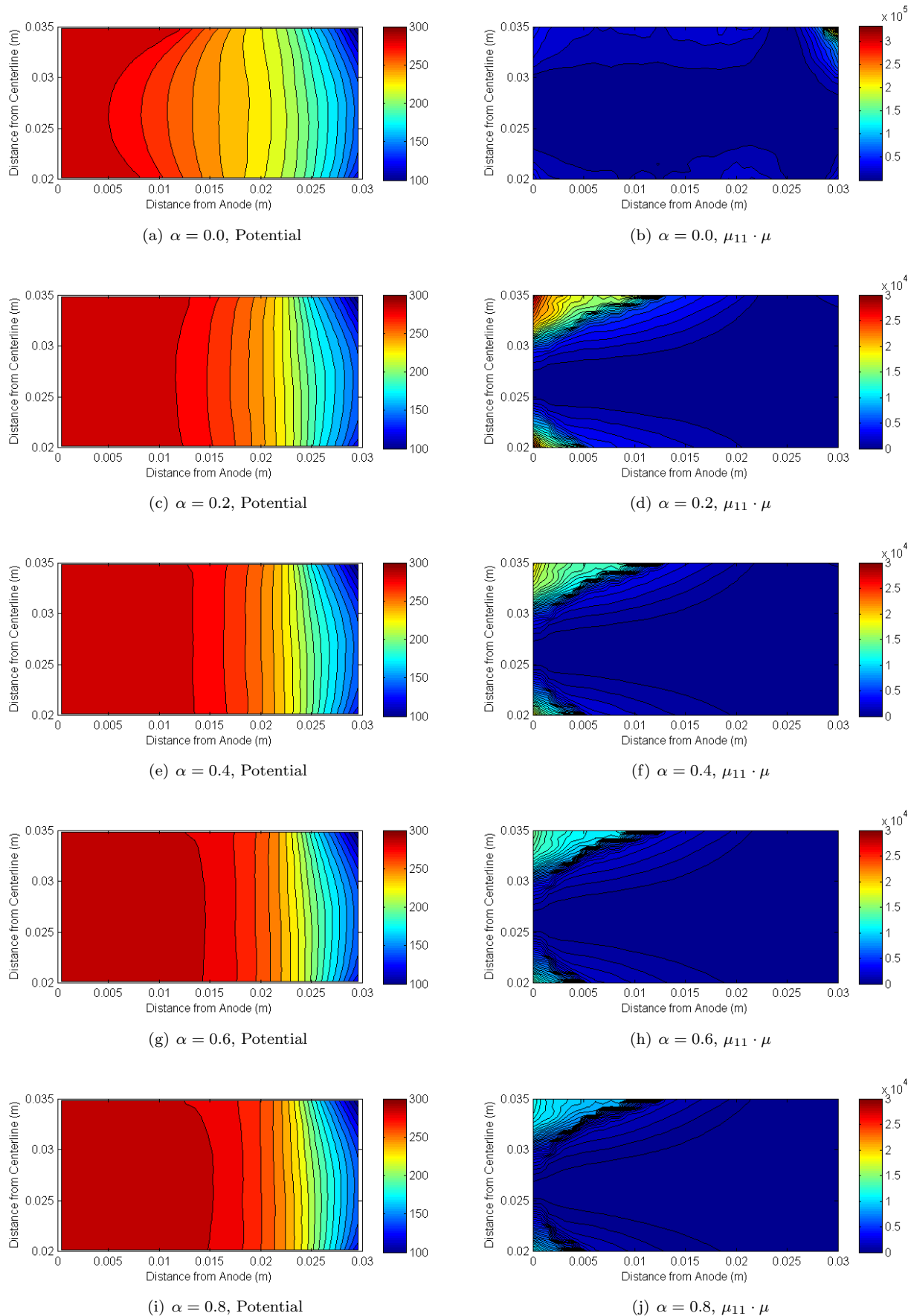
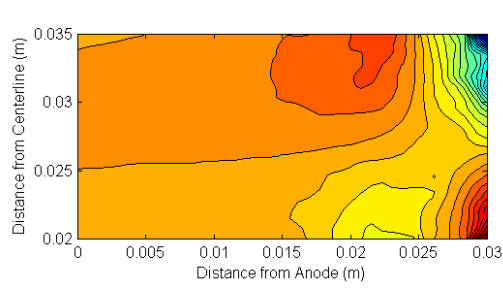
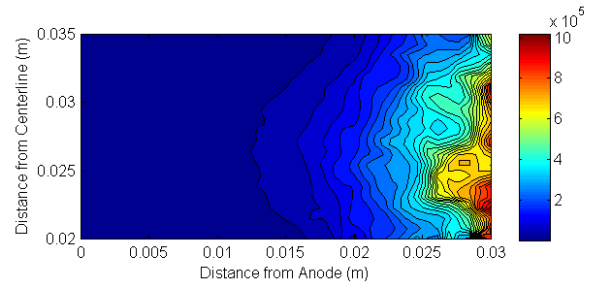


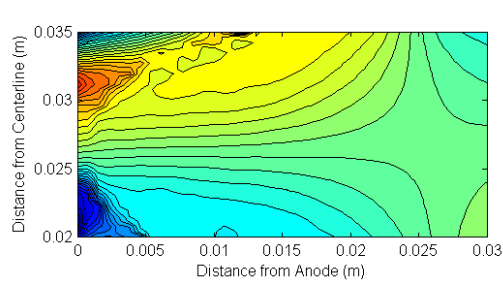
Figure 5. 2DFV Results (Part 1 of 2) (Note: Contour range not uniform)
9 of 14



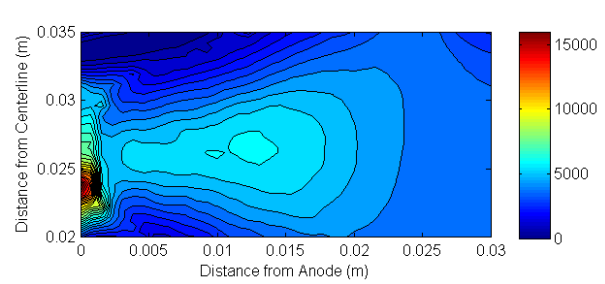
(a) $\alpha = 0.0, \mu_{12} \cdot \mu$



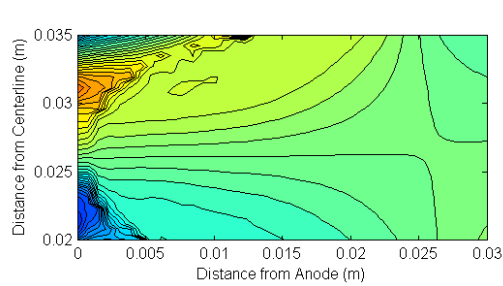
(b) $\alpha = 0.0, \mu_{22} \cdot \mu$



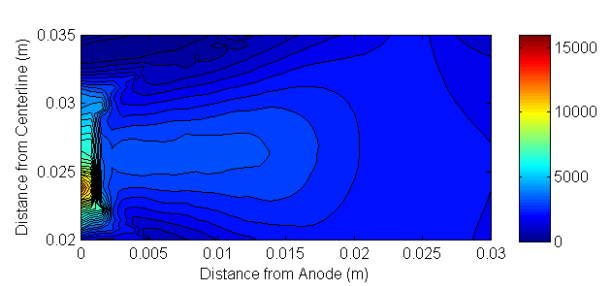
(c) $\alpha = 0.2, \mu_{12} \cdot \mu$



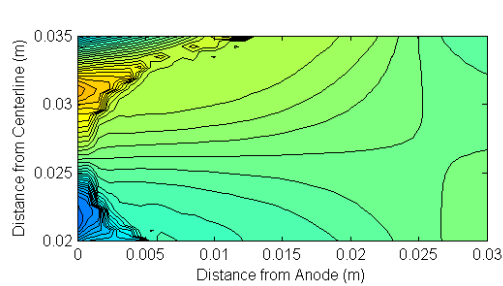
(d) $\alpha = 0.2, \mu_{22} \cdot \mu$



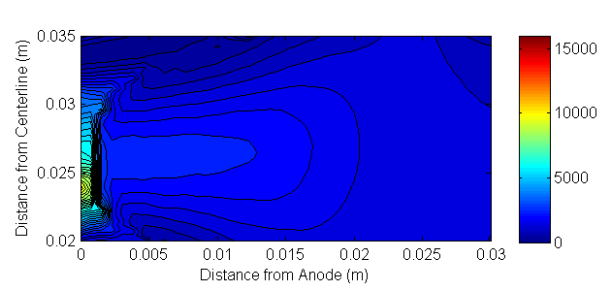
(e) $\alpha = 0.4, \mu_{12} \cdot \mu$



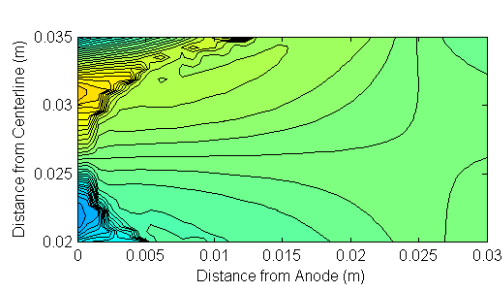
(f) $\alpha = 0.4, \mu_{22} \cdot \mu$



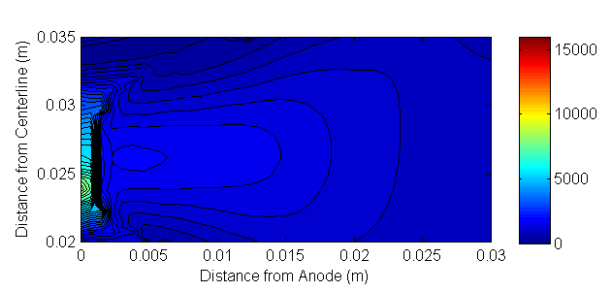
(g) $\alpha = 0.6, \mu_{12} \cdot \mu$



(h) $\alpha = 0.6, \mu_{22} \cdot \mu$



(i) $\alpha = 0.8, \mu_{12} \cdot \mu$



(j) $\alpha = 0.8, \mu_{22} \cdot \mu$

Figure 6. 2DFV Results (Part 2 of 2) (Note: Contour range not uniform)
10 of 14

Table 2. Hall current calculations

α	I_d (A)	$ I_{ExB} $ (A)	$ I_\theta $ (A)	Ω_{ExB}	Ω_θ
0.800	5.86	8.33	15.38	1.4	2.6
0.600	4.72	8.87	16.68	1.9	3.5
0.400	3.56	9.73	19.17	2.7	5.4
0.200	2.42	10.92	26.69	4.5	11.0
0.100	1.94	11.43	43.08	5.9	22.2
0.075	1.91	11.50	54.92	6.0	28.8
0.050	2.06	11.52	80.83	5.6	39.2
0.025	3.10	11.52	179.48	3.7	57.9
0.000	20.48	13.19	14404.00	0.6	703.3

using j_θ , the Hall current density (both positive and negative) is preferentially concentrated near the inner and outer dielectric walls. The large magnitude of the Hall current density in these regions is largely due to the high radial current densities near the walls.

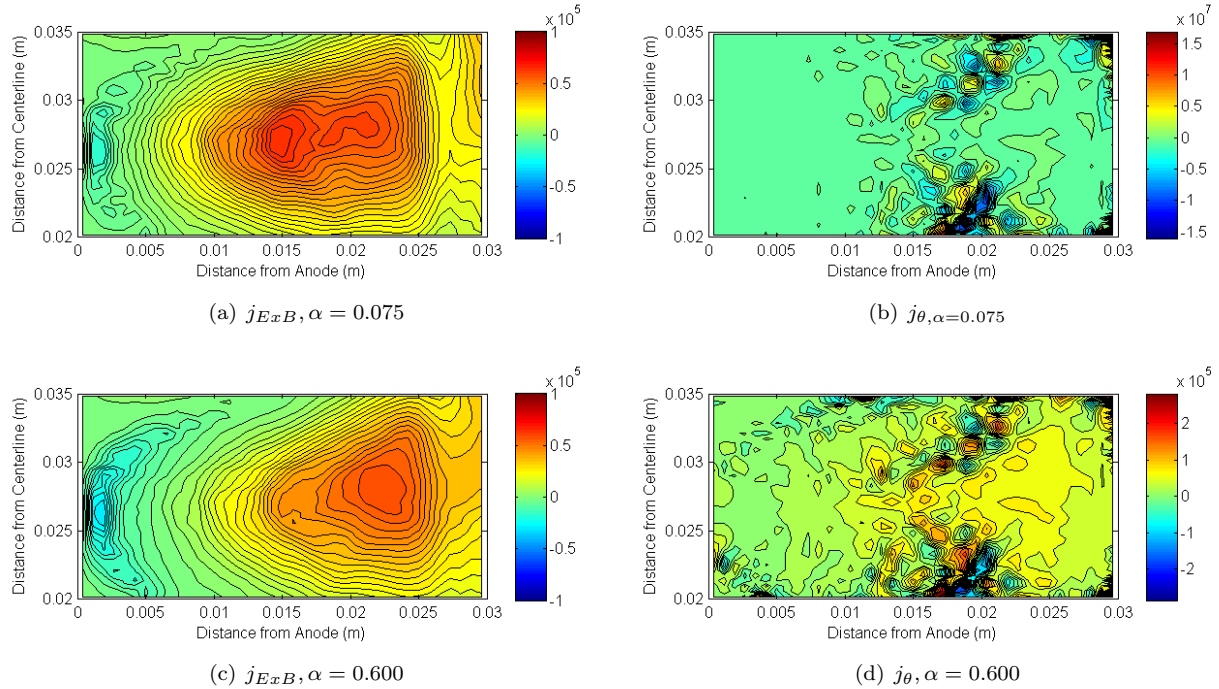


Figure 7. Hall current density profiles (Note: Contour range not uniform)

The significant differences in Hall current density behavior displayed by these results must be put into context. To begin, this particular plasma configuration (and the resulting Hall current profiles) are based on computational, rather than experimental, initial conditions. Furthermore, although this is a steady-state potential solver, the ability of the plasma to react to the electric field implies that this potential state is not necessarily a true steady-state configuration that might be observed experimentally. Even taking these considerations into account, some mechanism to account for anomalous transport without drastically modifying the electron mobility coefficient might help to reduce the discrepancy between the Hall current density results presented in this paper. An possible extension of this 2D axisymmetric formulation to account for $j \times B$ plasma turbulence effects directly is derived in Appendix A.

Further issues with the calculation of the Hall current from the j_{ExB} drift alone appear when considering an additional component to the azimuthal electron drift from the diamagnetic drift of the electrons:

$$v_{De} = \frac{\vec{\nabla} p \times \vec{B}}{q_e n_e B^2} \quad (27)$$

The calculated ExB and diamagnetic drifts for an $\alpha = 0.6$ simulation are provided in Fig. 8. The integrated ExB electron current, as shown in Table 2, is 8.87 A while the integrated diamagnetic electron current is -4.66 A. Close inspection of Fig. 8 shows that the diamagnetic current density peaks (negative) near the anode and while the ExB current density peaks (positive) much closer to the exit of the thruster. Again, in interpreting these results, it is crucial to understand that all results presented in this paper are based on a single set of computationally derived input data. For this case in particular, the very strong negative diamagnetic electron drift is likely due to the strong gradient in electron temperature near the anode seen Fig. 3(d). While the inclusion of the diamagnetic electron drift does little to explain the discrepancy between the j_θ and j_{ExB} drifts, the magnitude of the diamagnetic electron drift, even for this “non-experimental” case, indicates that it could be a significant drift mechanism in realistic discharge physics.

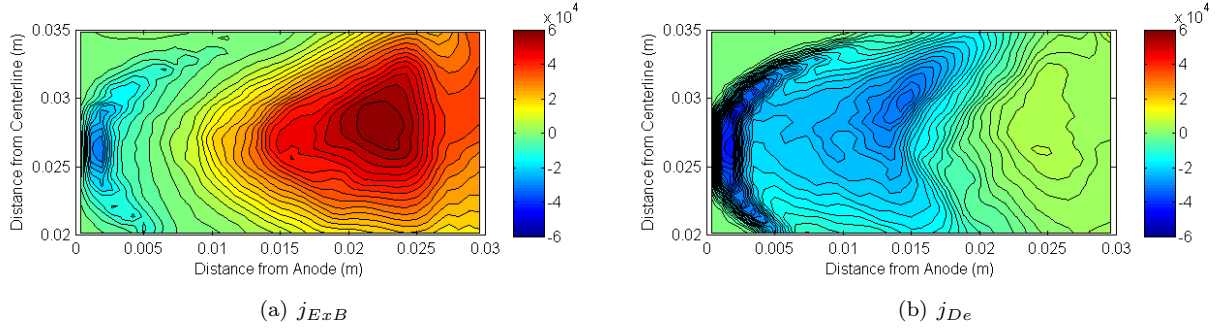


Figure 8. Classical fluid drifts perpendicular to B

VI. Conclusion

This work demonstrates the formulation of a finite-volume discretization scheme to solve a 2D axisymmetric version of the current conservation equation. The resulting simulation code, 2DFV, is used to model the acceleration channel of a Hall thruster. Performance of this code indicates that it is well suited to update existing quasi-1D potential solvers in hybrid PIC simulations (although a corresponding 2D electron energy solver is also desirable for true 2D capability). 2DFV results presented in this work display physically reasonable behavior in the limit of classical mobility and demonstrate a capacity to incorporate anomalous mobility corrections into the computational framework. Results provided indicate that strong discrepancies exist between the azimuthal electron current as calculated from the 2DFV framework and from the azimuthal component of the $\vec{E} \times \vec{B}$ drift. Finally, an extension of the 2D axisymmetric formulation to account for $j \times B$ plasma turbulence effects is proposed in Appendix A.

Appendix A - Formulation with plasma turbulence terms

Using basic concepts from linear perturbation theory, it is possible to include “plasma turbulence” terms into a Generalized Ohm’s law formulation by replacing individual field variables with a steady-state term plus a fluctuation term as follows (removing vector notation where applicable for simplicity):

$$\begin{aligned} j_e &= \bar{j}_e + j'_e \\ B &= \bar{B} + B' \\ E &= \bar{E} + E' \\ p &= \bar{p} + p' \end{aligned} \quad (28)$$

Plug these into the Eqn. 2 and taking the time average (note that the time average of the fluctuating

components is zero, so the electric field and pressure terms contain only steady state components) leaves the following formulation for the electron current density:

$$\vec{j}_e = \mu(\vec{j}_e \times \vec{B}) + \mu \langle j'_e \times B' \rangle + \mu ne \vec{E} + \mu \vec{\nabla} p \quad (29)$$

The additional cross correlation term, $\langle j'_e \times B' \rangle$, represents the time average of the cross product interaction between oscillations in the electron current density and the magnetic field. Depending on the particular model used to represent this term, it can provide a spatially varying positive, zero, or negative contribution to the electron current density. Modeling this term is beyond the scope of this effort; however, future research models for Bohm mobility should couple much more naturally with this approach than with 2DFV due to the explicit inclusion of these turbulent transport terms. To simplify the equation system, the $\langle j'_e \times B' \rangle$ term will be represented by the vector, $(\alpha_z, \alpha_r, \alpha_\theta)$, corresponding to the turbulent transport corrections in the three principal axes. Expanding the full electron current density equation, a set of three equations can be written for the electron current in the axial, radial, and azimuthal directions (dropping the subscript e for convenience).

$$\begin{aligned} j_z &= \mu(j_\theta B_r - j_r B_\theta + \alpha_z) + \mu ne E_z + \mu \nabla_z p \\ j_r &= \mu(j_z B_\theta - j_\theta B_z + \alpha_r) + \mu ne E_r + \mu \nabla_r p \\ j_\theta &= \mu(j_r B_z - j_z B_r + \alpha_\theta) + \mu ne E_\theta + \mu \nabla_\theta p \end{aligned} \quad (30)$$

Due to the axisymmetric geometry of the Hall thruster, the electric field and gradient of the pressure in azimuthal direction are identically zero. With this simplification, the azimuthal current is no longer a function of any azimuthal quantities and is written as:

$$j_\theta = \mu(j_r B_z - j_z B_r + \alpha_\theta) \quad (31)$$

Now it is possible to substitute j_θ into the equations for the axial and radial electron current density. This leads to the following set of coupled linear equations:

$$\begin{aligned} j_z &= \mu(\mu(j_r B_z - j_z B_r + \alpha_\theta) B_r - j_r B_\theta + \alpha_z) + \mu ne E_z + \mu \nabla_z p \\ j_r &= \mu(j_z B_\theta - \mu(j_r B_z - j_z B_r + \alpha_\theta) B_z + \alpha_r) + \mu ne E_r + \mu \nabla_r p \end{aligned} \quad (32)$$

This equation system can be solved to isolate the axial and radial components of the electric current density:

$$\begin{aligned} j_z &= \mu_{11}(\mu^2 \alpha_\theta B_r + \mu \alpha_z + \mu ne E_z + \mu \nabla_z p) \\ &\quad + \mu_{12}(\mu^2 \alpha_\theta B_z + \mu \alpha_r + \mu ne E_r + \mu \nabla_r p) \\ j_r &= \mu_{21}(\mu^2 \alpha_\theta B_r + \mu \alpha_z + \mu ne E_z + \mu \nabla_z p) \\ &\quad + \mu_{22}(\mu^2 \alpha_\theta B_z + \mu \alpha_r + \mu ne E_r + \mu \nabla_r p) \end{aligned} \quad (33)$$

Where the mobility coefficients are defined in Eqn. 8 and Eqn. 7 and the form for the azimuthal electron current is defined in Eqn. 31.

Appendix B - Convergence

Different L_2 norm convergence criteria are applied to a 40x40 node simulation with $\alpha = 0.6$. The resulting currents are provided in Table 3. To assess grid convergence, internal plasma quantities (electron temperature, ion velocity, plasma density, and neutral density) are linearly interpolated to the desired grid for a simulation with an L_2 norm convergence criteria of 0.001 and an anomalous correction of $\alpha = 0.6$. This use of interpolated plasma properties can be anticipated to perturb grid convergence; however, as the results in Table 4 demonstrate, approximate grid convergence can be achieved with a fine enough mesh. (Note: the 20x20 grid is very accurate because it does not require linear interpolation from the 40x40 grid.)

Table 3. L_2 norm convergence criteria

L_2 norm	I_e (A)	I_d (A)	Iterations	Time (sec)
10	3.4336	4.7393	200	6.1
1	3.4138	4.7195	316	9.7
0.1	3.4119	4.7175	430	13.1
0.01	3.4117	4.7173	546	16.3
0.001	3.4117	4.7173	660	19.8
0.0001	3.4117	4.7173	774	23.4

Table 4. Grid convergence criteria

Grid size	I_e (A)	I_d (A)
10x10	4.0189	5.3135
20x20	3.411	4.7156
25x25	3.4076	4.712
30x30	3.3825	4.6872
35x35	3.3859	4.6909
40x40	3.4117	4.7173

Acknowledgments

The author would like to thank Mr. Jung Yi for his assistance with gathering the HPHall data. The author would also like to thank the Dr. Douglas VanGilder and Lt. Lindell Pearson for monitoring this work. This work was funded under SBIR contract FA9300-06-D-0002.

References

- ¹J. M. Fife, Ph.D. thesis, Massachusetts Institute of Technology (1998)
- ²G. J. M. Hagelaar, J. Bareilles, L. Garrigues, and J.-P. Boeuf, *J. App. Phys.* 91, 5592 (2002)
- ³J. W. Koo and I. D. Boyd, *Comp. Phys. Comm.* 164, 442 (2004)
- ⁴A. I. Morozov and A. P. Shubin, *Sov. J. Plasma Phys.* 10, 728 (1984)
- ⁵J.-P. Boeuf and L. Garrigues, *J. App. Phys.* 84, 3541 (1998)